Stator Winding Temperature and Magnet Temperature Estimation of IPMSM Based on High-Frequency Voltage Signal Injection

Hwigon Kim, *Graduate Student Member, IEEE*, Hyun-Sam Jung, *Member, IEEE*, and Seung-Ki Sul, *Fellow, IEEE*

***Abstract*—The interior permanent-magnet synchronous motor (IPMSM) has been widely used as the traction motor in electric/hybrid vehicles because of its high torque density and wide operating speed range. During the operation of the IPMSM, the stator winding temperature and magnet temperature should be monitored to prevent winding insulation breakdown and irreversible demagnetization and to improve the torque accuracy. This article devised a method involving the use of a high-frequency (HF) resistance and an HF inductance for estimating these two temperatures at low motor speeds. The relationship between the HF impedance and both temperatures was determined and verified using an experimental setup in which both temperatures could be measured. Based on the relation, the temperature estimation method has been proposed, in this article, and verified by the experimental test. The proposed method was used to estimate the stator winding and the magnet temperatures simultaneously for 6000 s, and the maximum error was 6 °C and 3 °C for the stator winding and magnet temperature, respectively, even when the load and the temperatures varied considerably.**

***Index Terms*—High-frequency voltage injection, interior permanent-magnet synchronous motor (IPMSM), magnet temperature, temperature estimation, winding temperature.**

I. Introduction

THE interior permanent-magnet synchronous motor (IPMSM) is widely used in various applications such as robots and home appliances and in the automotive industry. In particular, following the development of electric vehicles, the IPMSM has been used as the traction motor in electric and hybrid vehicles over the past two decades, owing to its high torque density and wide operating speed range [1]. The IPMSM used in the automotive industry is designed to have a high power density, and the stator winding temperature is crucial information to prevent winding insulation breakdown. Furthermore, in servomotor and traction motor drives, the motor can operate with a current higher than the rated current for a short duration. Therefore, monitoring the stator winding temperature is imperative to maximize the operation area and to improve the motor dynamics without the winding insulation breaking down [2]–[5]. Accordingly, temperature sensors are attached to the stator winding to measure its temperature.

Estimation methods for the stator winding temperature have been developed to remove the stator winding temperature sensor or improve the sensor reliability. The methods are based on the principle that the stator winding resistance increases with the stator winding temperature. In [6], a dc stator current was injected into an induction machine to obtain the resistance variation. This method could estimate the resistance but caused torque pulsations. In another study, high-frequency (HF) impedance resulting from HF voltage injection was used to estimate the stator winding temperature for an induction motor [7]. Since the resistance variation of the stator winding influences the HF current harmonics induced by pulsewidth modulation (PWM), the variation of PWM-induced harmonics has also been used to estimate the winding temperature [3]. In this method, no additional signal is required, but high computation power is necessary. Another study estimated a dual three-phase permanent-magnet synchronous motor stator winding temperature by injecting an additional current at each d- and q-axis [8].

Additionally, the magnet temperature should also be monitored. A NdFeB magnet is generally used in the IPMSM for traction because of its high residual flux density and intrinsic coercivity, both of which decrease as the magnet temperature increases. Therefore, the magnet temperature should be monitored to prevent irreversible demagnetization and to improve the torque accuracy. However, it is difficult to measure the magnet temperature directly since the magnet is embedded in the rotor. Accordingly, noninvasive methods for magnet temperature estimation have been studied.

There are two types of methods to estimate the magnet temperature. In one type, based on a thermal model [9]–[11], the temperature of each motor part, including the stator winding,

Manuscript received 12 December 2021; revised 21 March 2022; accepted 29 April 2022. Date of publication 17 May 2022; date of current version 16 November 2022. This work was supported by the National Research Foundation of Korea (NRF) grant funded by the Korea Government (MSIT) (No.2021R1G1A1007687). *(Corresponding author: Hyun-Sam Jung.)*

Hwigon Kim and Seung-Ki Sul are with the Seoul National University, Seoul 08826, South Korea (e-mail: hwigon@eepel.snu.ac.kr; sulsk@snu.ac.kr).

Hyun-Sam Jung is with the Dongguk University, Seoul 04620, South Korea (e-mail: junghyunsam@dongguk.edu).

Color versions of one or more figures in this article are available at https://doi.org/10.1109/TIE.2022.3174285.

Digital Object Identifier 10.1109/TIE.2022.3174285

0278-0046 © 2022 IEEE. Personal use is permitted, but republication/redistribution requires IEEE permission.
See https://www.ieee.org/publications/rights/index.html for more information.

Authorized licensed use limited to: JACK YEH. Downloaded on September 23,2024 at 13:32:21 UTC from IEEE Xplore. Restrictions apply.

is estimated by solving a preconstructed thermal model of a motor on a testbed. However, owing to the complexity of the thermal model, extensive calibration, and a long commissioning time are required to achieve a reasonable estimation accuracy. Moreover, the estimation accuracy is highly dependent on the operating environment, such as a cooling system and a mechanical geometry.

The other type is based on an electrical model. Electrical-model-based methods can be classified based on the motor operating speed. The flux-based method can be used at medium and high speeds, where the voltage is sufficiently large to estimate the flux. This method uses the variation of either the magnet flux linkage [12], [13], or reactive power [14]–[16]. At low speeds, including standstill conditions, the flux-based method cannot be used since the terminal voltage is too small. Consequently, HF signal injection methods are used. In these methods, the variation in the HF resistance [17]–[20] is used to estimate the magnet temperature or magnetizing state. In [17], the magnet temperature of surface mounted permanent magnet synchronous machine (SMPMSM) was estimated using HF resistance. In [18], it was analyzed that the HF resistance is changed by permanent magnet magnetization state, which is decided by current. In the article, the effect was called magnetoresistance. In [19], the magnetoresistance in HF resistance was compensated when estimating the magnet temperature using HF resistance for SMPMSM and IPMSM. The stator winding temperature should be measured when the HF resistance is used in previous studies to decouple the stator winding resistance component from the HF resistance. Meanwhile, the HF inductance is used to estimate the magnet temperature [1], [21]–[23]. The HF inductance is independent of the resistance and can be used to estimate the magnet temperature precisely without information about the stator winding temperature.

The previous study [24] proposed the stator winding estimation method based on HF resistance. In addition to the previous study, this paper proposes a method for simultaneously estimating the stator winding and magnet temperatures at low speeds. In the proposed method, a pulsating HF voltage is injected at the *d*-axis in the rotor reference frame (RRF), and the HF inductance and resistance, i.e., HF impedance, are measured simultaneously. From these measurements, the stator winding temperature and magnet temperature estimation method is developed. Furthermore, the HF resistance and inductance calculation error due to the motor cross-coupling inductance and rotation speed is analyzed, and it is considered in developing the proposed method. Finally, the suitability of the proposed method for real-time estimation was experimentally verified. The stator winding and magnet temperature were accurately estimated online for 6000 s, even if the load and temperatures varied dynamically. The estimation error was less than 3 °C and 6 °C for the magnet and winding temperatures, respectively.

The rest of this article is organized as follows. In Section II, the correlation between HF resistance and winding temperature is discussed, and in Section III, the experimental setup used to verify the proposed method is briefly described. In Section IV, the HF impedance error due to the cross-coupling inductance and rotation speed is discussed. In Section V, the *d*-axis HF impedance extraction is configured, and it is applied to the experimental setup to validate the proposed method. In Section VI, the online temperature estimation result is explained. Finally, Section VII concludes this article.

II. HF Resistance and Stator Temperature

As mentioned, the stator winding resistance R_s is affected by the stator winding temperature ϑ_{sw} according to the relationship in

$$R_s\left(\vartheta_{\text{sw}}\right) = R_{s20}\left(1 + \alpha_{20}\left(\vartheta_{\text{sw}} - 20^{\circ}\text{C}\right)\right). \tag{1}$$

In this equation, Rs_{20} and α_{20} represent the stator winding resistance and the temperature coefficient of the winding material at 20 °C, respectively. Equation (2) describes an IPMSM model in the RRF

$$\mathbf{v}_{dqs}^{r} = R_s \mathbf{i}_{dqs}^{r} + \frac{d}{dt}\boldsymbol{\lambda}_{dqs}^{r} + \omega_r \mathbf{J} \cdot \boldsymbol{\lambda}_{dqs}^{r}. \tag{2}$$

Here, v is the voltage, i is the current, λ is the flux linkage, R_s is the stator resistance, ω_r is the electrical rotor speed, and the superscript "r" denotes the RRF. Boldface is used to represent a column vector quantity (e.g., $\mathbf{v}_{dqs}^{r} = [v_{ds}^{r} \;\; v_{qs}^{r}]^T$).

Furthermore, $\mathbf{J}$ is the 90° rotational transformation matrix defined as

$$\mathbf{J} \triangleq \begin{bmatrix} 0 & -1 \\ 1 & 0 \end{bmatrix}. \tag{3}$$

When an HF voltage signal is injected, the HF model in (4) can be derived from (2). In (4), $\mathbf{L}_{sh}$ and $\mathbf{R}_{sh}$ are the incremental inductance matrix and HF resistance matrix, respectively, and they are given by (5) and (6). In (6), the OFF-diagonal terms R_{dqh}, R_{qdh} come from the rotor resistance [25]

$$\mathbf{v}_{dqsh}^{r} = \mathbf{R}_{sh}\mathbf{i}_{dqsh}^{r} + \omega_r \mathbf{J}\mathbf{L}_{sh}\mathbf{i}_{dqsh}^{r} + \mathbf{L}_{sh}\frac{d}{dt}\mathbf{i}_{dqsh}^{r} \tag{4}$$

$$\mathbf{L}_{sh} \triangleq \begin{bmatrix} L_{dh} & L_{dqh} \\ L_{qdh} & L_{qh} \end{bmatrix} \tag{5}$$

$$\mathbf{R}_{sh} \triangleq \begin{bmatrix} R_{dh} & R_{dqh} \\ R_{qdh} & R_{qh} \end{bmatrix}. \tag{6}$$

Under the assumptions that the injected signal angular frequency ω_h is considerably higher than the rotation speed ω_r, (4) can be simplified as

$$\mathbf{v}_{dqsh}^{r} = \mathbf{R}_{sh}\mathbf{i}_{dqsh}^{r} + \mathbf{L}_{sh}\frac{d}{dt}\mathbf{i}_{dqsh}^{r}. \tag{7}$$

The *d*-axis HF equivalent circuit of the IPMSM based on (7) can be represented, as shown in Fig. 1 [1]. In the figure, the *d*-axis HF resistance comprises the winding resistance R_s, stator core loss $R_{\text{core|stator}}$, rotor core loss $R_{\text{core|rotor}}$, and magnet loss R_{magnet}. The resistance can be modeled as

$$R_{dh} = R_s + R_{\text{core}} + R_{\text{magnet}}. \tag{8}$$

The core loss depends on the motor speed, load condition, and magnet flux density, which is a function of the magnet temperature. It has been reported that magnet loss is influenced by the magnet temperature and load conditions [17]–[20], [26],

Authorized licensed use limited to: JACK YEH. Downloaded on September 23,2024 at 13:32:21 UTC from IEEE Xplore. Restrictions apply.

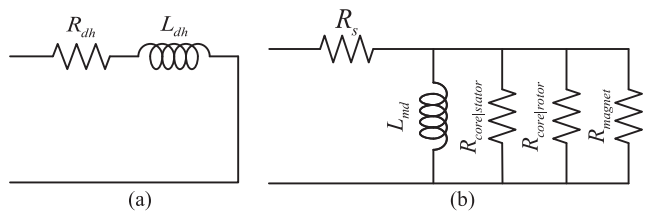

Fig. 1 *D*-axis high-frequency circuits. (a) Series lumped equivalent circuit. (b) *D*-axis high-frequency equivalent circuit.

[27]. Therefore, the d-axis HF resistance can be described as (9), where T_e, ω_r, ϑ_{sw}, and ϑ_{mag} represent the motor torque, rotation speed, stator winding temperature, and magnet temperature, respectively. The summation of core and magnet loss summation can be represented as a rotor resistance R_{dh_r}. In this article, the motor current was determined from the torque under the maximum torque per ampere (MTPA) operating condition

$$\begin{aligned} &R_{dh}\left(T_e,\,\omega_r,\vartheta_{\text{sw}},\vartheta_{mag}\right)\\ &= R_s\left(\vartheta_{\text{sw}}\right) + R_{\text{core}}\left(T_e,\,\omega_r,\vartheta_{mag}\right) + R_{\text{magnet}}\left(T_e,\omega_r,\vartheta_{mag}\right)\\ &= R_s\left(\vartheta_{\text{sw}}\right) + R_{dh_r}\left(T_e,\,\omega_r,\vartheta_{mag}\right). \end{aligned} \tag{9}$$

Previous research [17], [18], [20] reported that the rotor resistance varies according to the magnet temperature. The proposed winding temperature estimation method utilizes winding resistance R_s, variation in HF resistance R_{dh}. Since the rotor resistance in HF resistance is a function of the magnet temperature, the rotor resistance should be decoupled from the d-axis HF resistance to extract the winding resistance and estimate the winding temperature precisely. However, rotor resistance is difficult to measure, and its modeling is complicated.

Most IPMSM designs employ magnet segmentation, a flux barrier, and core lamination to reduce the magnet and core losses. With such loss-optimized designs, the magnet loss and core loss are considerably smaller than the conduction loss in low motor speeds [28], [29]. Hence, in this article, it is assumed that the core loss and magnet loss are small enough, and its variations due to the magnet temperature variation would be negligible. Also, under the assumption that magnet loss is considerably small, the cross-coupling resistance R_{dqh} and R_{qdh} in (6) are assumed as null.

The stator temperature estimation method devised in this article was developed under this approximation [24]. The validity of this assumption and the error resulting from the approximation was demonstrated experimentally and discussed in Section V.

III. Temperature Measurement System

A special rig was designed and developed, and it is shown in Fig. 2. In the rig, the stator winding temperature and magnet temperature of an IPMSM could be measured. Nine temperature sensors, represented by the green dots in Fig. 2, were attached to measure the stator winding temperature at each winding phase. The average of nine temperature sensor values is used as the stator winding temperature, though the difference in the temperature from each slot is small. Magnet temperatures were measured at 32 different locations on the magnets, and they are

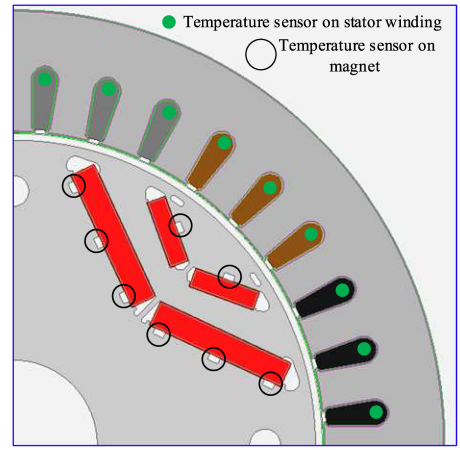

Fig. 2. Temperature sensor location on the winding and the magnet.

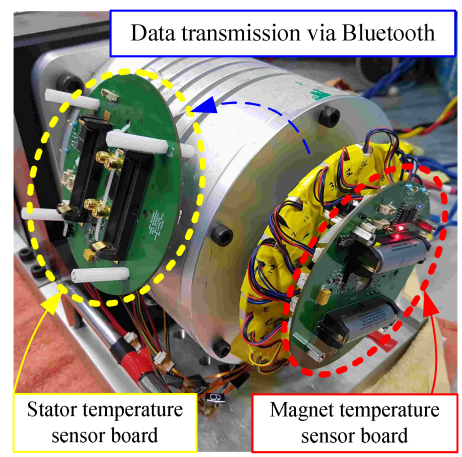

Fig. 3. Test motor with the temperature sensors.

indicated by the black circles in Fig. 2. The average of measured magnet temperatures is used as the magnet temperature. The magnet temperature sensors were connected to the magnet temperature sensor board, denoted by the red dashed line in Fig. 3. The magnet temperature sensor board rotated with the rotor, as shown in Fig. 3, and transferred the measured temperature value to the other board in the stationary part, which is encircled by the yellow dashed line in Fig. 3. The sensor board measured the stator winding temperature and transmitted all the temperature information to the control board. The error bound of the sensor is less than ±1.1 °C in the range from −50–150 °C [30]. The temperature measurement system consists of the current injection part, amplifier, analog-digital conversion part, and digital filter. The final error, including those signal processing parts, is less than ±1.5 °C. Each temperature is updated every 23 ms, which is small enough compared to the thermal time constant of the magnet and winding. The relation between stator resistance and the winding temperature was verified using the resistance meter RM3548 and the temperature measurement system. Fig. 4 shows the experimental results. The relation between resistance and temperature was well fitted by (1). Furthermore, R_{s20} and α_{20} were measured to be 1.424 Ω and 0.461%/°C, respectively.

Authorized licensed use limited to: JACK YEH. Downloaded on September 23,2024 at 13:32:21 UTC from IEEE Xplore. Restrictions apply.

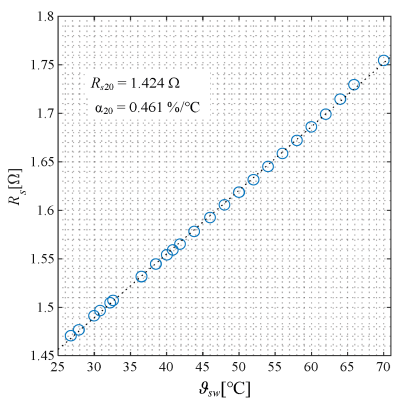

Fig. 4. Measured temperature and resistance of the stator winding.

TABLE I
PARAMETERS OF IPMSM

Parameter	Value
Poles	4
Rated current	9.4 A
Rated torque	10 N·m
Rated speed at 310 V dc link voltage	1800 r/min
Magnet flux linkage	0.369 V·s
Nominal stator winding resistance	1.4 Ω
Nominal L_{ds}	4.8 mH
Nominal L_{qs}	22 mH

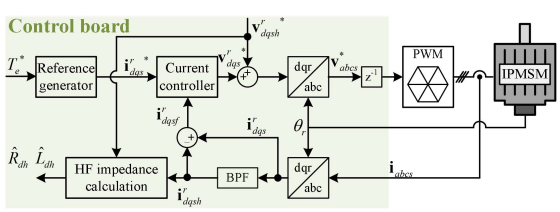

Fig. 5. Implementation of the HF voltage injection method.

The parameters of the IPMSM are listed in Table I. A detailed structure of the sensing system is described in [31].

This measurement system requires motor structure modification to measure the magnet temperature. An indirect measurement method in [14] can be applied if such modification is not allowed. In the indirect measurement method, magnet residual flux density calculated by q-axis voltage with no-load condition can be used to measure the magnet temperature indirectly [14].

IV. *D*-AXIS HF IMPEDANCE EXTRACTION

A. D-Axis HF Impedance Extraction by HF Voltage Injection

The d-axis HF impedance was extracted by injecting an additional HF voltage at the d-axis, as shown in Fig. 5. An HF voltage reference $\mathbf{v}^r_{dqsh}{}^*$, given by (10), was added to the current controller output $\mathbf{v}^r_{dqs}{}^*$

$$\mathbf{v}^r_{dqsh}{}^* = \begin{bmatrix} v^r_{dsh}{}^* \\ v^r_{qsh}{}^* \end{bmatrix} = V_h \begin{bmatrix} \cos\omega_h t \\ 0 \end{bmatrix}. \tag{10}$$

Here, V_h is the HF voltage magnitude, and ω_h is the HF signal angular frequency. The HF voltage induces an HF current $\mathbf{i}^r_{dqsh}$, which can be extracted using a bandpass filter whose center frequency is the injection frequency. The induced HF current can be expressed as

$$\mathbf{i}^r_{dqsh} = \begin{bmatrix} i^r_{dsh} \\ i^r_{qsh} \end{bmatrix} = \begin{bmatrix} I_{dh}\cos(\omega_h t + \varphi_d) \\ I_{qh}\cos(\omega_h t + \varphi_q) \end{bmatrix}. \tag{11}$$

Here, I_{xh} and φ_x represent the induced HF current magnitude and phase, respectively, where x is a specific axis between the d-axis and q-axis in the RRF. The parameters φ_x and I_{xh} are measured by demodulating the injected HF voltage reference and induced HF current [32]. The extracted φ_d and I_{dh} can be used to separate the d-axis HF impedance Z_{dh} into the inductance $\hat{L}_{dh}$ and resistance $\hat{R}_{dh}$ through (12), where cap symbol "^" denotes that these values are estimated

$$|Z_{dh}| = \frac{V_h}{I_{dh}}, \hat{L}_{dh} = -\frac{|Z_{dh}|}{\omega_h}\sin\varphi_d, \hat{R}_{dh} = |Z_{dh}|\cos\varphi_d. \tag{12}$$

Under the assumption that rotation speed ω_r is considerably lower than the injection frequency ω_h and that the cross-coupling inductance is sufficiently small that it can be neglected, the HF inductance and resistance calculated in (12) are equal to the real HF inductance L_{dh} and resistance R_{dh} in (5) and (6). However, the cross-coupling inductance cannot be neglected in highly saturated IPMSMs. Furthermore, the upper bound of the injection frequency is limited to several hundred hertz for the measurement of the HF resistance. Therefore, the estimated HF resistance $\hat{R}_{dh}$ in (12) could be different from the actual HF resistance. It will be discussed in the following section.

B. D-Axis HF Impedance Calculation Considering Cross-Coupling Inductance and Rotation Speed

This section discussed the HF impedance distortion caused by the cross-coupling inductance and rotation speed. For the discussion, the following equation is derived from (4)

$$\begin{bmatrix} v^r_{dsh} \\ v^r_{qsh} \end{bmatrix} = \left[\begin{bmatrix} R_{dh} - \omega_r L_{qdh} & -\omega_r L_{qh} \\ \omega_r L_{dh} & R_{qh} + \omega_r L_{dqh} \end{bmatrix} + j\omega_h \begin{bmatrix} L_{dh} & L_{dqh} \\ L_{qdh} & L_{qh} \end{bmatrix}\right] \begin{bmatrix} i^r_{dsh} \\ i^r_{qsh} \end{bmatrix}. \tag{13}$$

In this equation, there are two terms on the right-hand side. The first term comprises the HF resistance and HF inductance multiplied by the rotation speed, with the cross-coupling terms being diagonal elements. The second term is the HF inductance matrix multiplied by the injection frequency ω_h. Equation (13) can be represented as follows:

$$\begin{bmatrix} i^r_{dsh} \\ i^r_{qsh} \end{bmatrix} = \mathbf{Y}_h \begin{bmatrix} v^r_{dsh} \\ v^r_{qsh} \end{bmatrix} \tag{14}$$

where $\mathbf{Y}_\mathrm{h}$ is the admittance matrix given by

$$\mathbf{Y}_h \triangleq \begin{bmatrix} R_{dh} - \omega_r L_{qdh} + j\omega_h L_{dh} & -\omega_r L_{qh} + j\omega_h L_{dqh} \\ \omega_r L_{dh} + j\omega_h L_{qdh} & R_{qh} + \omega_r L_{dqh} + j\omega_h L_{qh} \end{bmatrix}^{-1}. \tag{15}$$

Authorized licensed use limited to: JACK YEH. Downloaded on September 23,2024 at 13:32:21 UTC from IEEE Xplore. Restrictions apply.

The estimated HF resistance and inductance can be calculated using (12) and represented, as shown in (17), as follows:

$$Z_{dh} \triangleq \left(\mathbf{Y}_h \begin{bmatrix} 1 \\ 0 \end{bmatrix} \begin{bmatrix} 1 & 0 \end{bmatrix}\right)^{-1} \tag{16}$$

$$\hat{R}_{dh} = \text{real}\left(Z_{dh}\right), \hat{L}_{dh} = imag\left(Z_{dh}\right). \tag{17}$$

Equation (17) can be expressed as (18) and (19) shown at the bottom of this page. As evident, the estimated HF resistance and inductance differ from the actual values because of the cross-coupling inductance L_{dqh} and rotation speed ω_r.

Finite element analysis (FEA) was performed to calculate the distortion caused by the cross-coupling inductance and rotation speed in the estimated HF resistance and inductance. The d-axis flux $\boldsymbol{\lambda}_{ds}^r$ and q-axis flux $\boldsymbol{\lambda}_{qs}^r$ were calculated by FEA at the various current level. The HF inductances were calculated by partial differentiation of the calculated fluxes by using

$$L_{dh} = \frac{\partial \lambda_{ds}^r}{\partial i_{ds}^r}, L_{qh} = \frac{\partial \lambda_{qs}^r}{\partial i_{qs}^r} \text{ and } L_{dqh} = L_{qdh} = \frac{\partial \lambda_{qs}^r}{\partial i_{ds}^r} = \frac{\partial \lambda_{ds}^r}{\partial i_{qs}^r}. \tag{20}$$

Fig. 6 shows the HF inductances L_{dh} and L_{qh} and the cross-coupling inductance L_{dqh} of the target motor in Fig. 2. The red dashed line denotes the MTPA operating point. Because of magnetic saturation, HF inductances vary with the current. Furthermore, the motor had nonnegligible cross-coupling inductance, similar to a traction motor.

Fig. 7 shows the distortion caused by cross-coupling inductance and rotation speed. Fig. 7(a) shows the difference between $\hat{R}_{dh}$ and R_{dh}, $R_{\text{dh_error}}$, and Fig. 7(b) shows the difference between $\hat{L}_{dh}$ and L_{dh}, $L_{\text{dh_error}}$. The speed ranged from 0 to 900 r/min, and the torque ranged from 0–10 N·m. The d-axis and q-axis currents were determined under the MTPA line in Fig. 6. The injection frequency was 500 Hz, and the actual HF resistances were assumed to be 1.45 Ω, which was the value of the stator winding resistance.

Estimated errors in the HF resistance and inductance shown in Fig. 7 are considerable. Significantly, the distortion of the HF resistance, the maximum error was about 14.5% of the actual value. The error increased with the load torque because the cross-coupling inductance increased with the current magnitude. Furthermore, the distortion became severe at a higher speed, as expected from (18). Therefore, the error in the HF resistance should be considered in the stator winding temperature estimation based on the estimated HF resistance. A previous study [20] estimated the magnet temperature from the HF resistance, and it compensated for the distortion by using a premeasured cross-coupling inductance look-up table (LUT) and injecting an additional HF signal at the q-axis. This article also assumed that measured HF inductances were identical to actual HF inductances. However, as shown in Fig. 7(b), the HF inductance varied by a maximum of 5% in the high torque region, and this assumption does not hold. Therefore, this article eliminated the distortion from the cross-coupling and rotation speed by constructing an LUT about the relation between HF resistance and winding temperature at each load torque and rotation speed. The experimentally measured distortion and the LUT are described in the following section.

V. Experimentally Measured *D*-Axis HF Impedance

This section discusses the experimental verification of the correlation between the HF resistance and the stator temperature in (1). Furthermore, based on an experimental result under various temperature conditions, it is demonstrated that the resistance variation caused by a variation in the magnet temperature is negligible. As mentioned in the previous section, the estimated HF resistance was affected by the load torque and rotation speed. This section presents experimental results that confirm it. On the basis of the analysis and observations, a method to estimate the stator winding temperature from the estimated d-axis HF resistance was developed.

A. Stator Winding Temperature and D-Axis HF Resistance

The HF impedance was measured at various operating points, magnet temperatures, and stator winding temperatures to determine the relationship between the d-axis HF resistance and the stator winding temperature. Motor operating points were determined by independently sweeping the rotation speed and load torque. The rotation speed was varied from 300–900 r/min at intervals of 150 r/min, and the torque was varied from 0 N·m to the rated value (10 N·m) at intervals of 1 N·m. HF current was measured at each operating point for ten periods of injection voltage. Each measurement at an operating point takes 20 ms. At the end of each measurement, motor temperatures were updated. The temperature variation during a measurement can be neglected, considering the thermal time constant of the motor.

Inverter nonlinearity effect caused by dead-time, parasitic capacitance, and voltage drop of the switching device distorts the output voltage of the inverter and the measured HF impedance. Fig. 8 shows the measured voltage distortion of the inverter used in the experiment. In the figure, the blue line denotes the output voltage distortion, and the red dashed line denotes the arctangent approximation in (21) [33]. In the equation, δV_{xn} and i_{xs} represent distortion voltage and phase current, where x

$$\hat{R}_{dh} = R_{dh} - \omega_r L_{qdh} + \frac{\left(\omega_r{}^2 L_{dh} L_{qh} + \omega_h{}^2 L_{dqh}{}^2\right)\left(R_{qh} + \omega_r L_{dqh}\right) + \omega_h \omega_r L_{dqh}\left(L_{qh} - L_{dh}\right)\left(\omega_h L_{qh}\right)}{\left(R_{qh} + \omega_r L_{dqh}\right)^2 + \left(\omega_h L_{qh}\right)^2} \tag{18}$$

$$\hat{L}_{dh} = L_{dh} + \frac{\omega_r L_{dqh}\left(R_{qh} + \omega_r L_{dqh}\right)\left(L_{qh} - L_{dh}\right) - L_{qh}\left(\left(\omega_r L_{dh}\right)\left(\omega_r L_{qh}\right) + \left(\omega_h L_{dqh}\right)^2\right)}{\left(R_{qh} + \omega_r L_{dqh}\right)^2 + \left(\omega_h L_{qh}\right)^2}. \tag{19}$$

Authorized licensed use limited to: JACK YEH. Downloaded on September 23,2024 at 13:32:21 UTC from IEEE Xplore. Restrictions apply.

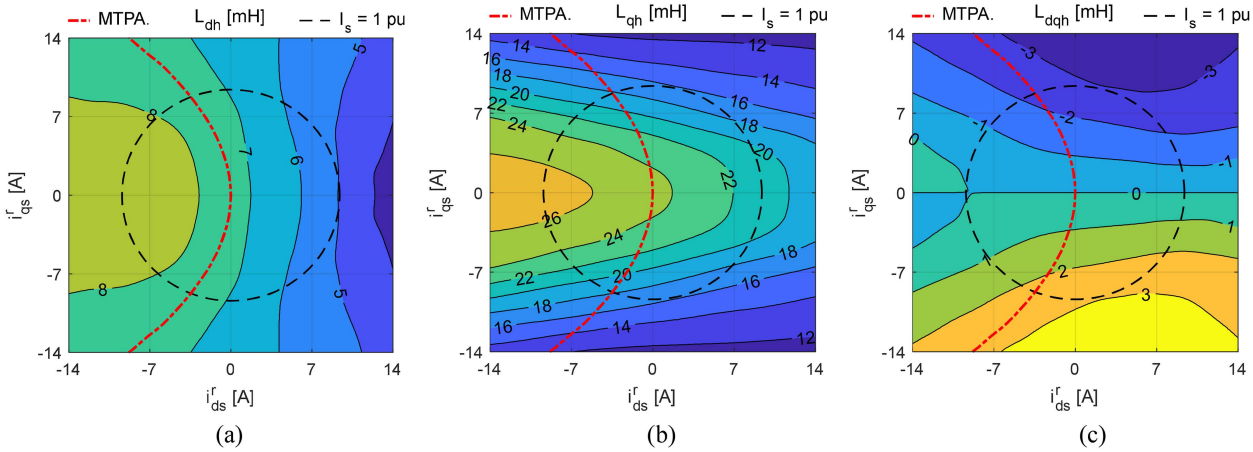

Fig. 6. HF inductances of the target IPMSM when the rotor is aligned to *d*-axis. (a) HF *d*-axis inductance. (b) HF *q*-axis inductance. (c) HF cross-coupling inductance.

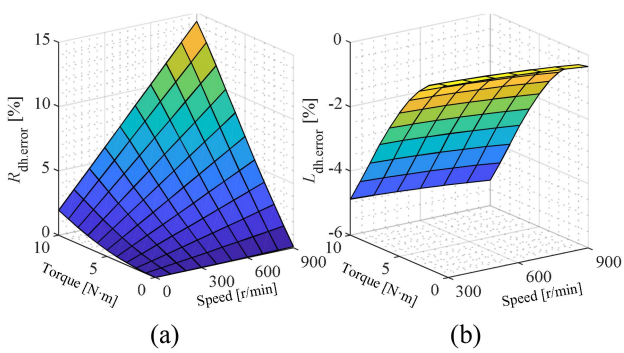

Fig. 7. Estimated HF impedance errors. (a) Resistance error. (b) Inductance error.

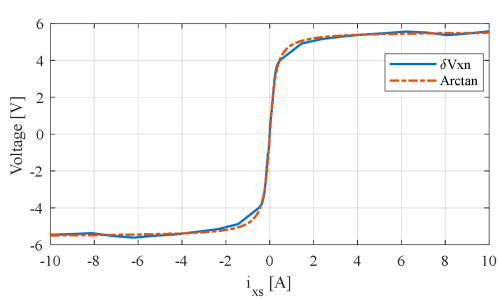

Fig. 8. Voltage distortion due to the inverter nonlinearity effect.

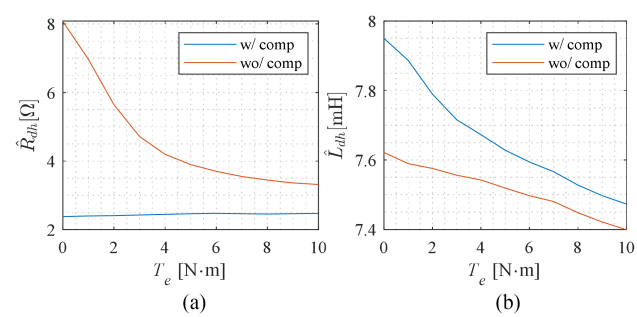

Fig. 9. Measured HF resistance and inductance with and without inverter nonlinearity compensation. (a) *D*-axis HF resistance. (b) *D*-axis HF inductance.

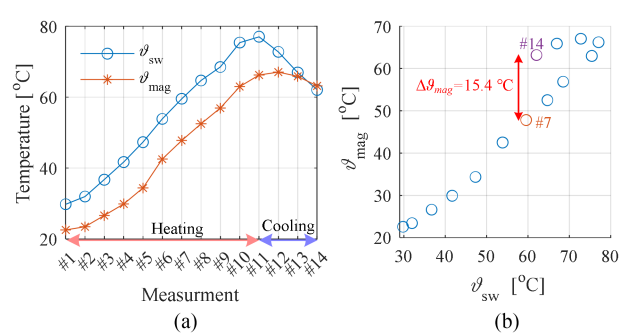

Fig. 10. Magnet and winding temperatures at each measurement. (a) Time series plot. (b) Scattered plot.

is an arbitrary phase in a, b, and c

$$\delta V_{xn} = \frac{2}{\pi} V_{sat} \text{atan}\left(K_{\text{atan}} \cdot i_{xs}\right). \tag{21}$$

Fig. 9 shows the measured HF resistance and inductance of the target motor, where the blue and red line represent the HF impedance with the compensation in (21) and without compensation, respectively. The figure reveals that HF voltage should be appropriately compensated. Without compensation, the measured HF resistance and inductance would be distorted.

A total of 14 measurements were performed at an operating point for the increasing and decreasing phases of the motor temperature to measure the HF impedance in various temperature conditions. Fig. 10(a) shows the stator winding temperature and rotor magnet temperature at each measurement; #*n* denotes the *n*th measurement. The motor temperature increased from the first to the eleventh measurement, called a heating sequence. In the heating sequence, the stator winding temperature was higher than the magnet temperature, and the winding and magnet temperatures increased from 28–77 °C and 22–67 °C, respectively.

Authorized licensed use limited to: JACK YEH. Downloaded on September 23,2024 at 13:32:21 UTC from IEEE Xplore. Restrictions apply.

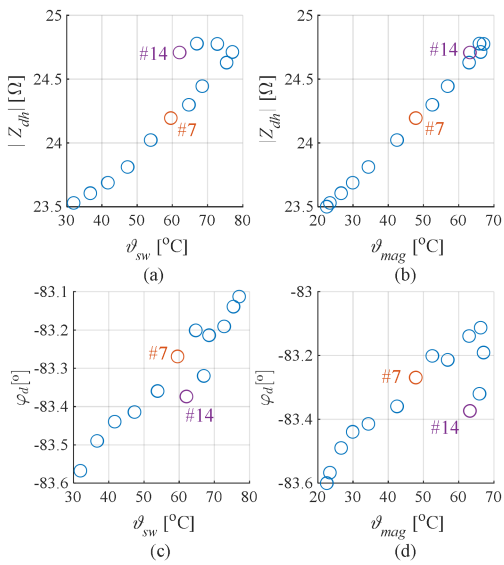

Fig. 11. Measured magnitude and phase of the HF impedance plotted against the stator winding and magnet temperatures. (a) Magnitude versus the winding temperature. (b) Magnitude versus the magnet temperature. (c) Phase versus the winding temperature. (d) Phase versus the magnet temperature.

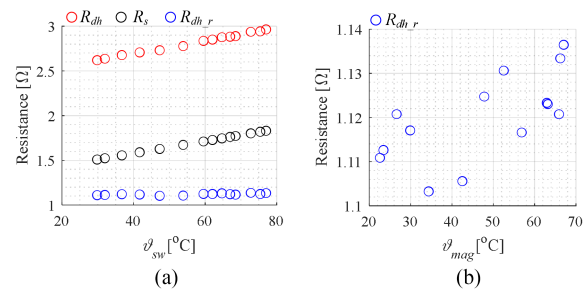

Fig. 12. HF resistance at 900 r/min, 10 N·m. (a) Each component in *d*-axis HF resistance variation according to the winding temperature. (b) Rotor resistance variation according to the magnet temperature.

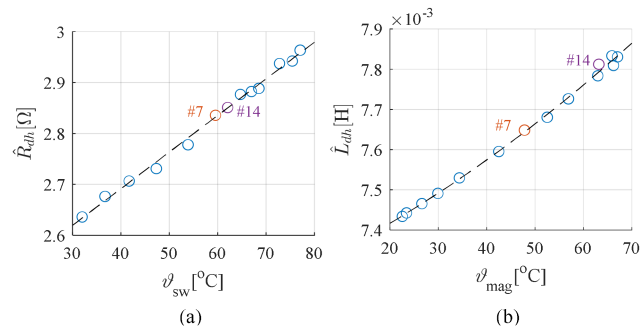

Fig. 13. Measured *d*-axis HF resistance and inductance at 10 N·m and 900 r/min. (a) Resistance. (b) Inductance.

The motor was cooled by an external cooling system from the eleventh to the fourteenth measurement. This cooling is referred to as a cooling sequence. In this sequence, the winding temperature decreased more rapidly than the magnet temperature, and both temperatures decreased about 60 °C. The impedance at various temperature combinations could be obtained from HF impedances measured in both sequences. Fig. 10(b) shows the winding and magnet temperatures in a scatter plot. The seventh and 14th measurements are denoted by orange and purple circles, respectively. These two points have different magnet temperatures 47.6 °C and 63.3 °C for the same stator temperature 59 °C. The magnet temperature difference is 15.4 °C.

Fig. 11 shows the measured *d*-axis impedance by the motor temperature for a load torque of 10 N·m and a rotation speed of 900 r/min; #*n* denotes the *n*th measurement, and it corresponds to Fig. 10. Fig. 11(a) and (b) shows the variation of the *d*-axis impedance magnitude with the winding and magnet temperatures, respectively, and Fig. 11(c) and (d) shows the variation of the impedance phase with the winding and magnet temperatures, respectively. In this article, the impedance magnitude and impedance phase were calculated by demodulating the induced *d*-axis HF current. From the measured impedance magnitude and phase in Fig. 11, the *d*-axis HF resistance and *d*-axis HF inductance variation by the winding or magnet temperature can be determined.

Fig. 12 shows the measured R_{dh}, which was calculated using (12) and the measured HF impedance magnitude and phase in Fig. 11. In the figure, the red circle denotes the measured HF resistance. The black circle denotes the R_s, calculated using measured winding temperature and (1). The blue circle denotes the HF rotor resistance R_{dh_r} calculated by subtracting R_s from the R_{dh}. Fig. 12(b) shows the HF rotor resistance variation by the magnet temperature. The figure shows that the magnet temperature rarely changes the HF resistance. This result shows the validity of the assumption that the HF resistance variation with the stator temperature is much more dominant than the HF resistance variation with the magnet temperature.

Fig. 13(a) shows the variation of the HF resistance with the stator winding temperature. In Fig. 13(a), the estimated HF resistance varies linearly with the stator winding temperature. A comparison of the estimated HF resistance at two points, #7 and #14, shows that HF resistance is rarely changed by the magnet temperature. Thus, the estimated HF resistance is affected not by the magnet temperature but by the stator temperature for given torque and speed. Therefore, the HF resistance could be used to estimate the winding temperature regardless of the magnet temperature. On the basis of the experimental result, the *d*-axis HF resistance was modeled as (22). In the equation, the *d*-axis HF resistance is a function of the winding temperature since the magnet temperature effect on the *d*-axis HF resistance is negligible

$$\begin{aligned} R_{dh}\left(\vartheta_{\mathrm{sw}}\right)\big|_{T_e,\omega} &= R_{\mathrm{sw}}\left(\vartheta_{\mathrm{sw}}\right) + R_{\mathrm{core}}\big|_{T_e,\omega} + R_{\mathrm{magnet}} \\ &= R_{dh0}\big|_{T_e,\omega}\left(1 + \alpha\big|_{T_e,\omega}\left(\vartheta_{\mathrm{sw}} - 20\,^{\circ}\mathrm{C}\right)\right). \end{aligned} \tag{22}$$

Fig. 13(b) shows the variation of the HF inductance with the magnet temperature, calculated from the impedance magnitude and phase in Fig. 11(b) and (d). Clearly, the HF inductance varies with the magnet temperature, and it is independent of the stator

Authorized licensed use limited to: JACK YEH. Downloaded on September 23,2024 at 13:32:21 UTC from IEEE Xplore. Restrictions apply.

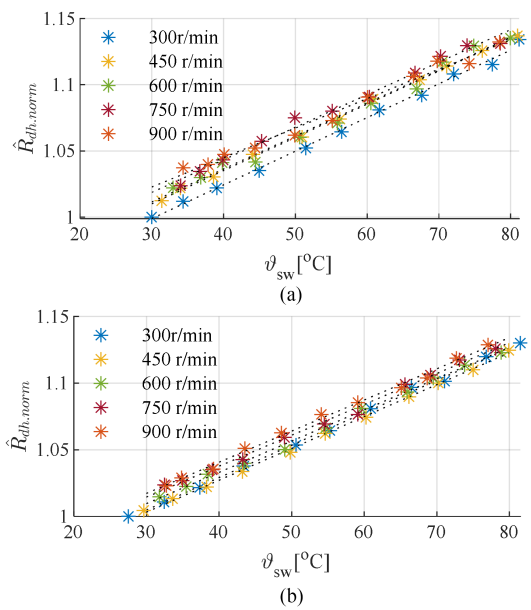

Fig. 14. Measured *d*-axis HF resistance at various motor speeds at (a) 10 N·m and (b) 5 N·m.

winding temperature [1], [21]–[23]. The relationship between the magnet temperature and HF inductance in Fig. 13(b) was modeled as a second-order polynomial [21]

$$L_{dh}\left(\vartheta_{mag}\right)|_{T_e,\omega} = \mathrm{A}|_{T_e,\omega}\vartheta_{mag}{}^2 + \mathrm{B}|_{T_e,\omega}\vartheta_{mag} + \mathrm{C}|_{T_e,\omega}. \tag{23}$$

As explained in the previous section, $\hat{R}_{dh}$ and $\hat{L}_{dh}$ varied not only with the motor temperature but also with the load torque and speed. Therefore, $R_{dh0}|_{T_e,\omega}$ and $\alpha|_{T_e,\omega}$ in (22) were calculated through linear regression at each load torque and speed. Similarly, $\mathrm{A}|_{T_e,\omega}$, $\mathrm{B}|_{T_e,\omega}$, and $\mathrm{C}|_{T_e,\omega}$in (23) were calculated at each load torque and speed.

B. Measured D-Axis HF Resistance and Motor Operating Conditions

Fig. 14 shows the normalized measured *d*-axis HF resistance at various speeds for load torques of 10 and 5 N·m. Clearly, the HF resistance increases linearly with the stator winding temperature at every speed and load torque. Evidently, the estimated *d*-axis HF resistance increased with the motor speed for a given winding temperature. This is because $\hat{R}_{dh}$ varies because of the distortion effect analyzed in Section IV. A comparison of Fig. 14(a) and (b) shows that the variation of the HF resistance with the motor speed is more significant at the higher torque, as expected from Fig. 7.

VI. Online Stator Temperature Estimation

A. Online Temperature Estimator and Look-Up Tables

The proposed method estimates the winding and magnet temperature by comparing HF resistance and inductance with preconstructed LUTs. A simple temperature estimator can be designed as follows. Fig. 15 shows a control block diagram for

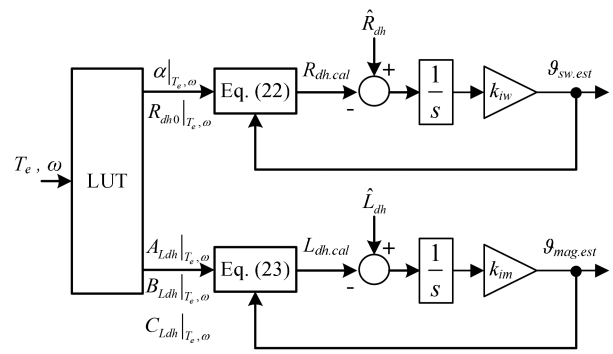

Fig. 15. Motor temperature estimator.

simultaneous winding and magnet temperature estimation. The estimator involves LUTs, (22), (23), and integrators.

From the coefficient obtained from the LUT and the estimated winding temperature, the *d*-axis HF resistance is calculated using (22). Then, the integrator output would be the estimated winding temperature. The closed-loop transfer function of the winding temperature estimator is as follows:

$$\frac{\vartheta_{\mathrm{sw}.est}}{\vartheta_{\mathrm{sw}}} = \frac{R_{dh0}|_{T_e,\omega}\,\alpha|_{T_e,\omega}k_{iw}}{s + R_{dh0}|_{T_e,\omega}\,\alpha|_{T_e,\omega}k_{iw}}. \tag{24}$$

The designed estimator is a first-order low-pass filter whose bandwidth is $R_{dh0}|_{T_e,\omega}\alpha|_{T_e,\omega}k_{iw}$. The integrator gain k_{iw} can be adjusted according to the load condition to maintain the estimator bandwidth at 10 Hz. Similarly, the magnet temperature estimator is implemented [21]. The closed-loop transfer function of the magnet temperature estimator can be deduced as follows, and the bandwidth of the estimator is also set to 10 Hz:

$$\frac{\vartheta_{mag.est}}{\vartheta_{mag}} = \frac{\left(\mathrm{A}|_{T_e,\omega}\vartheta_{mag} + \mathrm{B}|_{T_e,\omega}\right)k_{im}}{s + \left(\mathrm{A}|_{T_e,\omega}\vartheta_{mag} + \mathrm{B}|_{T_e,\omega}\right)k_{im}}. \tag{25}$$

B. Online Estimation Results

An online estimation experiment was performed for 6000 s, as shown in Fig. 16(a). Because of the memory limit in an oscilloscope, the experiment was performed in 2000 s divisions and each part of the experiment is labeled as #1, #2, and #3 in the figure. The magnet temperature and stator winding temperature show a jump between each execution since it took a few minutes to store the data.

The winding temperature varied from 36–84 °C, and the magnet temperature varied from 33–70 °C. The stator winding temperature was dynamically changed by modifying the load torque command to verify the proposed method. The speed was also changed dynamically to verify the proposed method for various speed conditions.

At various speeds and torques, the winding temperature was estimated within a maximum error of 6 °C, and the magnet temperature was estimated within a maximum error 3 °C, except for the spikes in the transient. At various temperature conditions, regardless of whether the temperature increased or decreased, the proposed method estimated the winding and magnet

Authorized licensed use limited to: JACK YEH. Downloaded on September 23,2024 at 13:32:21 UTC from IEEE Xplore. Restrictions apply.

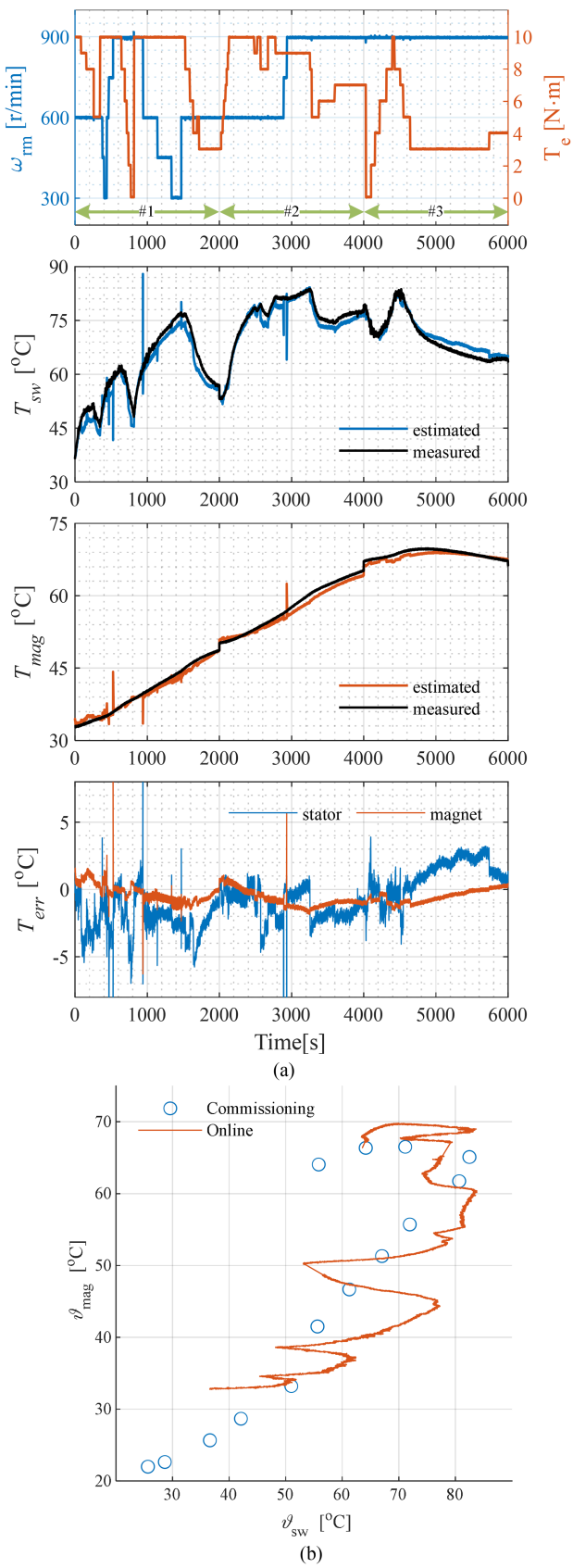

Fig. 16. Online temperature estimation result. (a) Load condition, stator winding temperature, magnet temperature, and estimation error. (b) Temperature trajectory.

temperature simultaneously. Fig. 16(b) shows the temperature trajectory. The blue circles indicate the temperature condition at the commissioning state, which were used to generate the LUT, and the orange line denotes the temperature trajectory for the online estimation. As shown in the figure, the proposed method was verified in various temperature conditions where the difference between the stator winding temperature and the magnet temperature was over 33 °C. The results shows that the modeling of HF resistance and inductance about the winding and magnet temperature holds outside of the temperature conditions explored in the commissioning. The online estimation showed that the winding temperature estimation error resulting from magnet temperature variations was negligible. Furthermore, the magnet temperature estimation error resulting from the stator winding temperature variation was also negligible.

VII. Conclusion

This article proposed a method for the simultaneous estimation of the stator winding and magnet temperatures based on the *d*-axis HF resistance and *d*-axis HF inductance. The relation between the *d*-axis HF impedance and these two temperatures was analyzed by using an experimental setup in which the stator winding temperature and magnet temperature could be simultaneously measured. From experimental results, it was shown that the HF resistance was rarely changed by magnet temperature. The results were contrary to the previous studies, which estimate the magnet temperature using HF resistance. The difference with previous studies comes from the loss minimized motor design.

From the HF voltage equation of the IPMSM, the HF resistance and inductance estimation error caused by the cross-coupling inductance and nonzero rotation speed were theoretically analyzed. The estimation error was verified by using FEA and experimental results.

The winding and magnet temperatures were simultaneously estimated by the developed estimator. Online temperature estimation was performed for 6000 s under conditions where the torque, speed, winding temperature, and magnet temperature varied dynamically, and the maximum temperature difference between the stator winding and magnet exceeded 33 °C. Throughout the test period, the estimation error was less than 6 °C and 3 °C for the stator winding and magnet temperature, respectively. Though the proposed method has been verified with the IPMSM, the method can be equally applied to the SMPMSM.

The limitation of the proposed method is that the method requires additional HF voltage signal injection. Therefore, the method can only be applicable in low-speed, where dc-link voltage is sufficient to synthesize the HF voltage. Also, if the motor has a lot of spatial harmonics, this method cannot be applied at standstill. Furthermore, HF current induced by HF voltage causes additional losses and audible noise. In addition, offline data collection is required to implement this method. However, the offline test for the proposed method is simpler than the thermal model-based methods since the HF impedance

Authorized licensed use limited to: JACK YEH. Downloaded on September 23,2024 at 13:32:21 UTC from IEEE Xplore. Restrictions apply.

model exploited in this method can be represented as a simple function such as a first- and second-order polynomial.

References

[1] H. Jung, D. Park, H. Kim, S. Sul, and D. J. Berry, "Non-invasive magnet temperature estimation of IPMSM based on high-frequency inductance with a pulsating high-frequency voltage signal injection," *IEEE Trans. Ind. Appl.,* vol. 55, no. 3, pp. 3076–3086, May/Jun. 2019.

[2] S. D. Wilson, P. Stewart, and B. P. Taylor, "Methods of resistance estimation in permanent magnet synchronous motors for real-time thermal management," *IEEE Trans. Energy Convers.,* vol. 25, no. 3, pp. 698–707, Sep. 2010.

[3] N. Z. Popov, S. N. Vukosavic, and E. Levi, "Motor temperature monitoring based on impedance estimation at PWM frequencies," *IEEE Trans. Energy Convers.,* vol. 29, no. 1, pp. 215–223, Mar. 2014.

[4] C. Kral, A. Haumer, and S. B. Lee, "A practical thermal model for the estimation of permanent magnet and stator winding temperatures," *IEEE Trans. Power Electron.,* vol. 29, no. 1, pp. 455–464, Jan. 2014.

[5] L. He, S. Cheng, Y. Du, R. G. Harley, and T. G. Habetler, "Stator temperature estimation of direct-torque-controlled induction machines via active flux or torque injection," *IEEE Trans. Power Electron.,* vol. 30, no. 2, pp. 888–899, Feb. 2015.

[6] L. Sang-Bin and T. G. Habetler, "An online stator winding resistance estimation technique for temperature monitoring of line-connected induction machines," *IEEE Trans. Ind. Appl.,* vol. 39, no. 3, pp. 685–694, May/Jun. 2003.

[7] F. Briz, M. W. Degner, J. M. Guerrero, and A. B. Diez, "Temperature estimation in inverter-fed machines using high-frequency carrier signal injection," *IEEE Trans. Ind. Appl.,* vol. 44, no. 3, pp. 799–808, May/Jun. 2008.

[8] Z. Li, G. Feng, C. Lai, W. Li, and N. C. Kar, "Current injection-based simultaneous stator winding and PM temperature estimation for dual three-phase PMSMs," *IEEE Trans. Ind. Appl.,* vol. 57, no. 5, pp. 4933–4945, Sep./Oct. 2021.

[9] T. Huber, W. Peters, and J. Böcker, "Monitoring critical temperatures in permanent magnet synchronous motors using low-order thermal models," in *Proc. Int. Power Electron. Conf.*, 2014, pp. 1508–1515.

[10] G. D. Demetriades, H. Z. d. l. Parra, E. Andersson, and H. Olsson, "A real-time thermal model of a permanent-magnet synchronous motor," *IEEE Trans. Power Electron.,* vol. 25, no. 2, pp. 463–474, Feb. 2010.

[11] N. Simpson, R. Wrobel, and P. H. Mellor, "An accurate mesh-based equivalent circuit approach to thermal modeling," *IEEE Trans. Magn.,* vol. 50, no. 2, pp. 269–272, Feb. 2014.

[12] A. Specht and J. Böcker, "Observer for the rotor temperature of IPMSM," in *Proc. 14th Int. Power Electron. Motion Control Conf.*, 2010, pp. T4-12–T4-15.

[13] G. Feng, C. Lai, J. Tjong, and N. C. Kar, "Non-invasive kalman filter based permanent magnet temperature estimation for permanent magnet synchronous machines," *IEEE Trans. Power Electron.,* vol. 33, no. 12, pp. 10673–10682, Dec. 2018.

[14] H. S. Jung, H. Kim, S. K. Sul, and D. J. Berry, "Permanent magnet temperature estimation in a mass-produced traction motor for an electric vehicle," *IEEE Trans. Transp. Electrific.*, vol. 8, no. 2, pp. 1863–1873, Jun. 2022.

[15] H. S. Jung, H. Kim, S. K. Sul, and D. J. Berry, "Temperature estimation of IPMSM by using fundamental reactive energy considering variation of inductances," *IEEE Trans. Power Electron.,* vol. 36, no. 5, pp. 5771–5783, May 2021.

[16] H. S. Jung, H. Kim, S. K. Sul, and D. J. Berry, "Magnet temperature estimation of IPMSM by using reactive energy," in *Proc.10th Int. Conf. Power Electron. ECCE Asia*, 2019, pp. 1–6.

[17] D. D. Reigosa, F. Briz, P. García, J. M. Guerrero, and M. W. Degner, "Magnet temperature estimation in surface PM machines using high-frequency signal injection," *IEEE Trans. Ind. Appl.,* vol. 46, no. 4, pp. 1468–1475, Jul./Aug. 2010.

[18] D. D. Reigosa, D. Fernandez, Z. Zhu, and F. Briz, "PMSM magnetization state estimation based on stator-reflected PM resistance using high-frequency signal injection," *IEEE Trans. Ind. Appl.,* vol. 51, no. 5, pp. 3800–3810, Sep./Oct. 2015.

[19] D. D. Reigosa, D. Fernandez, H. Yoshida, T. Kato, and F. Briz, "Permanent-magnet temperature estimation in PMSMs using pulsating high-frequency current injection," *IEEE Trans. Ind. Appl.,* vol. 51, no. 4, pp. 3159–3168, Jul./Aug. 2015.

[20] G. Feng, C. Lai, K. L. V. Iyer, and N. C. Kar, "Improved high-frequency voltage injection based permanent magnet temperature estimation for PMSM condition monitoring for EV applications," *IEEE Trans. Veh. Technol.,* vol. 67, no. 1, pp. 216–225, Jan. 2018.

[21] H. S. Jung, D. Park, H. Kim, S. K. Sul, and D. J. Berry, "Non-invasive magnet temperature estimation in IPMSM by high frequency pulsating sinusoidal voltage injection," in *Proc. IEEE Transp. Electrific. Conf. Expo*, 2018, pp. 858–862.

[22] D. Reigosa, D. Fernández, M. Martínez, J. M. Guerrero, A. B. Diez, and F. Briz, "Magnet temperature estimation in permanent magnet synchronous machines using the high frequency inductance," *IEEE Trans. Ind. Appl.,* vol. 55, no. 3, pp. 2750–2757, May/Jun. 2019.

[23] H. S. Jung, H. Kim, S. K. Sul, and D. J. Berry, "Magnet temperature estimation of traction motor in standstill with considering spatial harmonics," *IEEE Trans. Ind. Electron.,* vol. 68, no. 11, pp. 10546–10557, Nov. 2021.

[24] H. Kim, H. S. Jung, and S. K. Sul, "Stator winding temperature estimation of IPMSM based on a high-frequency voltage signal injection," in *Proc. IEEE Conf. Transp. Electrific. Expo*, 2020, pp. 896–900.

[25] L. Alberti, N. Bianchi, and S. Bolognani, "High-frequency d-q model of synchronous machines for sensorless control," *IEEE Trans. Ind. Appl.,* vol. 51, no. 5, pp. 3923–3931, Sep./Oct. 2015.

[26] K. Atallah, D. Howe, P. H. Mellor, and D. A. Stone, "Rotor loss in permanent-magnet brushless ac machines," *IEEE Trans. Ind. Appl.,* vol. 36, no. 6, pp. 1612–1618, Nov./Dec. 2000.

[27] K. Yamazaki and A. Abe, "Loss investigation of interior permanent-magnet motors considering carrier harmonics and magnet eddy currents," *IEEE Trans. Ind. Appl.,* vol. 45, no. 2, pp. 659–665, Mar./Apr. 2009.

[28] K. Yamazaki and H. Ishigami, "Rotor-shape optimization of interior-permanent-magnet motors to reduce harmonic iron losses," *IEEE Trans. Ind. Electron.,* vol. 57, no. 1, pp. 61–69, Jan. 2010.

[29] K. Yamazaki and Y. Fukushima, "Effect of eddy-current loss reduction by magnet segmentation in synchronous motors with concentrated windings," *IEEE Trans. Ind. Appl.,* vol. 47, no. 2, pp. 779–788, Mar./Apr. 2011.

[30] "Temperature dependent platinum thin film chip resistor (RTD)," *Vishay*. Accessed: Mar. 21, 2022. [Online]. Available: https://www.vishay.com/docs/28762/ptsserie.pdf

[31] D. Park, H. S. Jung, H. Cho, and S. K. Sul, "Design of wireless temperature monitoring system for measurement of magnet temperature of IPMSM," in *Proc. IEEE Transp. Electrific. Conf. Expo*, 2018, pp. 656–661.

[32] P. L. Jansen and R. D. Lorenz, "Transducerless position and velocity estimation in induction and salient ac machines," *IEEE Trans. Ind. Appl.,* vol. 31, no. 2, pp. 240–247, Mar./Apr. 1995.

[33] D. Kim, Y. Kwon, S. K. Sul, J. Kim, and R. Yu, "Suppression of injection voltage disturbance for high-frequency square-wave injection sensorless drive with regulation of induced high-frequency current ripple," *IEEE Trans. Ind. Appl.,* vol. 52, no. 1, pp. 302–312, Jan./Feb. 2016.

Hwigon Kim (Graduate Student Member, IEEE) received the B.S. degree in electrical engineering and computer science in 2018 from Seoul National University, Seoul, South Korea, where he is currently working toward Ph.D. degree in electrical engineering.

His current research interests include control of power electronics and its application for electrical machines.

Authorized licensed use limited to: JACK YEH. Downloaded on September 23,2024 at 13:32:21 UTC from IEEE Xplore. Restrictions apply.

Hyun-Sam Jung (Member, IEEE) received the B.S., M.S., and Ph.D. degrees in electrical engineering and computer science from Seoul National University, Seoul, South Korea, in 2010, 2012, and 2019, respectively.

From 2012 to 2015, he was with Samsung Heavy Industries Company Ltd., Suwon, South Korea. From 2019 to 2020, he was with LG Electronics, Inc., Seoul, South Korea. Since 2020, he has been an Assistant Professor with the Division of Electronics and Electrical Engineering, Dongguk University, Seoul, South Korea. His current research interests include power electronics, control of electrical machines, and power-converter circuits.

Seung-Ki Sul (Fellow, IEEE) received the B.S., M.S., and Ph.D. degrees in electrical engineering from Seoul National University, Seoul, South Korea, in 1980, 1983, and 1986, respectively.

From 1986 to 1988, he was an Associate Researcher with the Department of Electrical and Computer Engineering, University of Wisconsin, Madison, WI, USA. From 1988 to 1990, he was a Principal Research Engineer with LG Industrial Systems Company, South Korea. Since 1991, he has been a faculty member with the School of Electrical and Computer Engineering, Seoul National University, where he is currently a Professor leading the Power Electronics Lab, Seoul National University. He has authored or coauthored more than 160 IEEE journal papers and a total of more than 350 international conference papers in the area of power electronics. His current research interests include position sensorless control of electrical machines, electric/hybrid vehicles and ship drives, and power-converter circuits based on SiC MOSFET.

Dr. Sul was the Program Chair of IEEE Power Electronics Specialists Conference in 2006 and the General Chair of IEEE International Conference on Power Electronics and ECCE-Asia in 2011. From 2011 to 2014, he was the Editor-in-Chief for the Journal of Power Electronics, an SCIE-registered journal published by the Korean Institute of Power Electronics (KIPE), Seoul, South Korea. For the year 2015, he was the President of KIPE. He was simultaneously the recipient of the 2015 IEEE Transaction first and second Paper Awards on Industrial Application. He was also the recipient of the 2016 Outstanding Achievement Award of the IEEE Industrial Application Society. He was also selected as the recipient of the 2017 Newell award sponsored by IEEE Power Electronics Society.

Authorized licensed use limited to: JACK YEH. Downloaded on September 23,2024 at 13:32:21 UTC from IEEE Xplore. Restrictions apply.